RSC Advances

PAPER

Check for updates

Macro/microbehavior of shale rock under the dynamic impingement of a high-pressure supercritical carbon dioxide jet

Fei Huang [ID] *[ab] and Bin Hu[c]

This paper focuses on the damage of shale rock impacted by a high-pressure supercritical carbon dioxide (SC-CO_2) jet. A well-designed apparatus was used to conduct experiments with a high-pressure SC-CO_2 jet impacting shale core plugs. The damage, including the macrofailure and the microchanges of shale samples, was analyzed. The results show that the shale cores develop grid-like fractures on the top surface, while many layered fractures were observed inside the shale cores by means of computed tomography scan. The maximum broken depth of the shale core plugs is dependent upon the combined actions of jet pressure, jet temperature and target distance. The scanning electron microscope images along with the X-ray diffraction results indicate that the shale samples are eroded by the SC-CO_2 jet. This erosion may further lead to the macrodamage of shale samples by reducing their mechanical strength.

1. Introduction

Shale gas is one of the most important alternative sources of conventional natural gas. It is known that shale gas reservoirs are characterized by low porosity and low permeability. Reservoir reconstruction must be carried out to extract shale gas. Currently, hydraulic fracturing technology is the main method for reforming shale reservoirs. However, some disadvantages may restrict the wide use of this method: (i) the high content of clay minerals in shale may cause hydrophilic expansion,[1] which will cause drilling tools to jam; (ii) the shortage of water resources is another disadvantage; and (iii) the pollution of groundwater by fracturing fluid may cause harm to the environment.[2] To overcome the above disadvantages, some special fracturing fluids, such as polymer microsphere emulsion[3] and bio-degradable oligo,[4] have received increasing attention.

SC-CO_2 is a type of material in an unconventional phase state. Its density is close to liquid, while its viscosity is close to gas.[5] It does not cause clay expansion in the absence of water. Meanwhile, the shale samples absorb SC-CO_2 more easily than methane gas. This will cause the sequestration of carbon dioxide and desorption of natural gas.[6] Due to the foregoing advantages, SC-CO_2 is considered to be an ideal fluid for jet fracturing the shale gas reservoir.[7,8] Therefore, the failure laws

of shale subjected to the SC-CO_2 jet are of great scientific significance.

Kolle used SC-CO_2 jets to assist coiled tubing drilling experiments. His results revealed that the SC-CO_2 jet can effectively reduce the threshold pressure for rock breaking.[9] Du carried out experimental studies on the fracturing of rock with the SC-CO_2 jet. The results also showed that the SC-CO_2 jet can effectively reduce the rock breaking threshold pressure and cause massive rock crushing.[10] Wang conducted the same experiments.[11] His results demonstrated that pump pressure, jet temperature, confining pressure, jet distance, rotary speed of core samples and jet time are the main factors influencing the rock-breaking performance and efficiency. Except for the physical impacts, the research results of Li and Jing[12] indicated that SC-CO_2 immersion will cause damage to the rock and reduce the rock's physical strength. Guo *et al.*[13] found that the mechanical properties of shale rock soaked with SC-CO_2 were largely dependent upon the pressure of SC-CO_2. Zhang *et al.*[14] conducted simulation experiments on SC-CO_2 fracturing in shale. They found that fracturing using SC-CO_2 can reduce the pressure needed to initiate fractures by more than 50%. This subject was also studied by Hu *et al.*[15] Lu *et al.*[16] conducted experimental studies on the swelling of shale in supercritical carbon dioxide, which has important consequences with regard to the production of shale gas and the sequestration of CO_2 in shale formations. Zhang *et al.*[17] found that significant surface structural changes occurred in shale after saturation with CO_2 and brine, and an obvious decrease in the uniaxial compressive strength of shale was observed.

Most of the above studies put their weight on the changes of shale rock subjected to static SC-CO_2 fluid. Although some studies have been conducted to research the impact of high-

[a]Work Safety Key Lab on Prevention and Control of Gas and Roof Disasters for Southern Coal Mines, Hunan University of Science and Technology, Xiangtan, Hunan 411201, China. E-mail: fhuang@hnust.edu.cn

[b]Hunan Provincial Key Laboratory of Safe Mining Techniques of Coal Mines, Hunan University of Science and Technology, Xiangtan, Hunan 411201, China

[c]School of Resource Environment and Safety Engineering, Hunan University of Science and Technology, Xiangtan, Hunan 411201, China

pressure SC-CO$_2$ jet on the changes of rock samples, few studies take shale rock as the experimental sample. This paper plans to study the failure mechanism of shale samples impacted by a SC-CO$_2$ jet at both the macroscopic and microscopic levels.

2. Materials and methods

2.1. Shale samples

Typical shale samples were collected from the Longmaxi Formation of Sichuan Basin's lower Silurian series in the southeastern Chongqing area of China. To keep in line with the actual engineering conditions, the shale samples were tested under undrained conditions. The combined test results of total organic carbon (TOC), thermal maturity (R_0) and porosity of the shale in this region indicate that the reservoir is rich in shale gas.[18] Moreover, this region has been widely considered to be China's largest and most favorable area for shale gas accumulation.[19,20] X-ray diffraction (XRD) analysis shows that the mineral components of the shale mainly consist of quartz, lay minerals (including chlorite, kaolinite and illite), calcite and dolomite. The mass percentages of these components are 52%, 27%, 11% and 9%, respectively.

The shale samples were first collected from the outcrop, and then the core plugs were drilled with water from these large blocks of shale. The size of the core plug is 100 millimeters in diameter and 150–250 millimeters in length. Computerized tomography (CT) can be utilized to obtain the internal characteristics of the rock in a nondestructive manner.[21] Fig. 1 shows the CT images of the shale core plugs. According to the CT images, it can be observed that the bedding of the shale is well developed. Multiple bedding planes are approximately parallel to each other.

2.2. SC-CO$_2$ jet impacting rock apparatus

The experimental SC-CO$_2$ jet breaking rock apparatus consists of four independent units: a storage unit, a modulation unit, a rock breaking unit, and a recovery unit. The storage unit mainly consists of a CO$_2$ tank and a CO$_2$ supplement device. It is used for the long-term storage of liquid CO$_2$. The CO$_2$ pressure in the container is kept in 3.0–5.0 MPa. The temperature in the tank is kept within a range of −15 to 5 °C. The CO$_2$ supplement device can complement the loss of CO$_2$ during the experiments. The modulation unit mainly consists of a plunger pump and

a heater. First, the liquid CO$_2$ is pumped out from the tank and pressurized to the experiment's required pressure. Then, it is heated to the required temperature. Using the above procedure, supercritical CO$_2$ can be created. The experimental unit is illustrated schematically in Fig. 2. It is primarily used to form the SC-CO$_2$ jet and to conduct rock breaking experiments. After modulation, the supercritical CO$_2$ enters the main unit of the rock breaking system through the wellbore inlet. Then, the SC-CO$_2$ is jetting out from the nozzle. The SC-CO$_2$ jet will impact the rock cores at the bottom. Finally, the SC-CO$_2$ will flow into the next unit through the outlet. The recovery unit consists of a solid separator, a liquid separator and a refrigerator. Its main functions are to separate CO$_2$ from the rock debris mixture after the experiments (i.e., to remove debris, water and other impurities). Then, the clean CO$_2$ is converted to liquid form and transported back to the CO$_2$ tank.

2.3. Experimental procedure

This experiment is mainly intended to study the influence of the pump pressure on the rock-breaking performance. Based on the threshold pressure[22] required for rock breaking, pump pressures of 30, 35, 40, 45, 50, and 55 MPa are selected as the experimental pressures. To maintain the supercritical phase of CO$_2$, the temperature of the heater is a variable ranging from 35 °C to 80 °C. The nozzle with an outlet diameter of 2 millimeters is selected. An optimal target distance range of 1 mm to 12 mm is selected according to the findings of Du et al.[10] The experimental time was set to 3 minutes for each experimental pressure. Fig. 3 shows the pump pressure changing processes over time. This demonstrates that each experimental pressure sustains approximately 3 minutes. Plunger pump 1 is selected to pressurize the liquid CO$_2$. In this experiment, we assume that the embedded depth of shale rock is about 400 m and the mean density is about 2000 kg m^{-3}. So a confinement pressure of 8 MPa is selected to monitor the deep condition of shale rock. The detailed test parameters are listed in Table 1.

Firstly, the shale core was wrapped with a Teflon tube. A heat gun was used to shrink the Teflon material in order to keep the shale core wrapped tightly enough. Then the wrapped core was put into the core holder as shown in Fig. 2. Plenty of hydraulic fluid was pumped into the gaps between core holder and Teflon tube until the confinement pressure climbed to ∼8 MPa. This
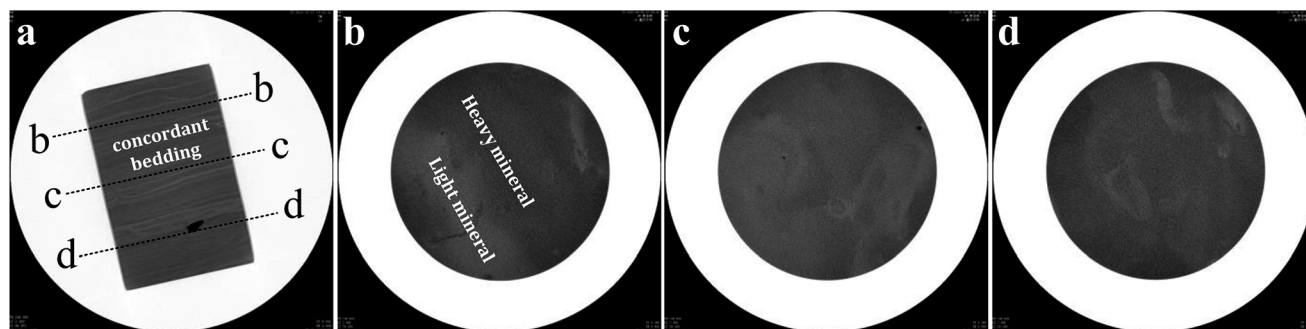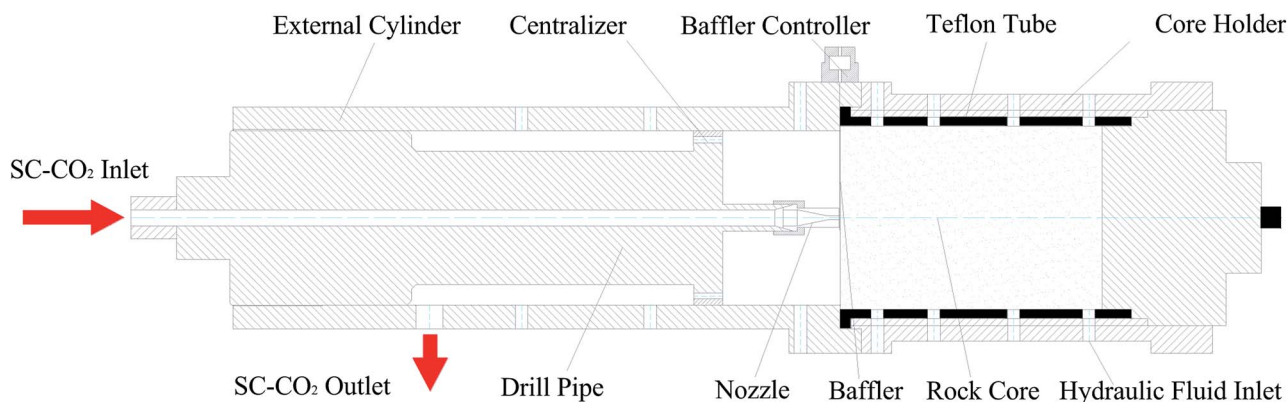

Fig. 1 CT images of shale core plugs.

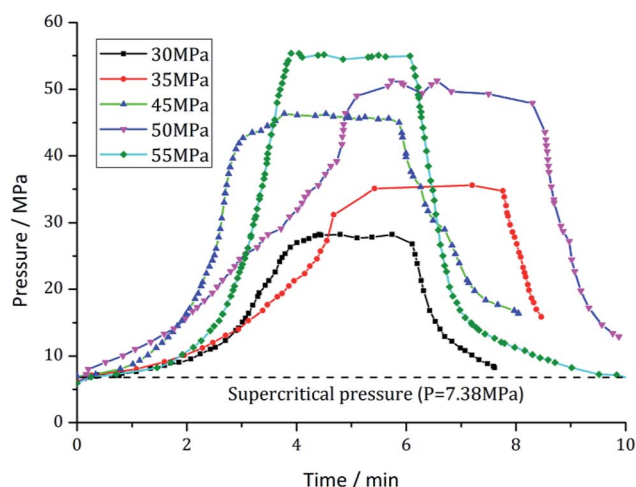**Fig. 2** Schematic diagram of the SC-CO$_2$ jet impacting rock apparatus.

Fig. 3 The changing curves of pump pressures over time.

confinement pressure can prevent the incursion of SC-CO$_2$ of which the pressure in the annular space was measured much lower than ~5 MPa. Thirdly, the baffler was withdrawn and the SC-CO$_2$ jet impacted onto the top surface of shale core. After the impacting, the wrapped shale core was taken down for further test.

3. Results and discussions

3.1. The macrofailure of shale

Fig. 4 and 5 show the pictures of shale core plugs impacted by the SC-CO$_2$ jet. It presents a grid-like fragmentation phenomenon on the top surface. When the pump pressure is 30 MPa, no crack

appears on the core's end face. Increasing the pump pressure to over 35 MPa, some tiny cracks form in the central area. These initial cracks then extend along the radial direction to the free surface. Multiple cracks connect to each other during crack propagation. Then, cracks in the grid pattern appeared, as shown in Fig. 4. This grid-crack phenomenon becomes increasingly obvious with increasing pump pressure. Finally, shale core plugs may suffer from grid-like massive fracture morphology. From the macroscopic phenomenon in Fig. 4, it can be obtained that the threshold pressure of the shale breaking by the SC-CO$_2$ jet is approximately between 30 and 35 MPa.

Computed tomography (CT) scan images show that multiple transverse cracks are generated inside the shale cores shown in Fig. 5. These cracks are parallel to the shale bedding. It is analyzed that they may be caused by the stress waves induced by the impact of the SC-CO$_2$ jet. Once the transverse cracks extend through the rock, the shale debris will be peeled off. Then, the shale core plugs will present what is known as the mass-broken morphology shown in Fig. 4. This morphology is identical to that described in the existing literature.[8,11]

Giving a certain pump pressure, the rock damage will roughly extend to a maximum depth (Δh). Fig. 6 indicates that the damage depth increases linearly with the increasing pump pressure. A linear relationship between Δh and pressures can be described as follows:

$$\Delta h = -64.4 + 2.2P \tag{1}$$

where P is the pump pressure. The fitting correlation coefficient of the formula is $R^2 = 0.9878$. From eqn (1), it can be inferred

Table 1 Summary of the test constant and variables

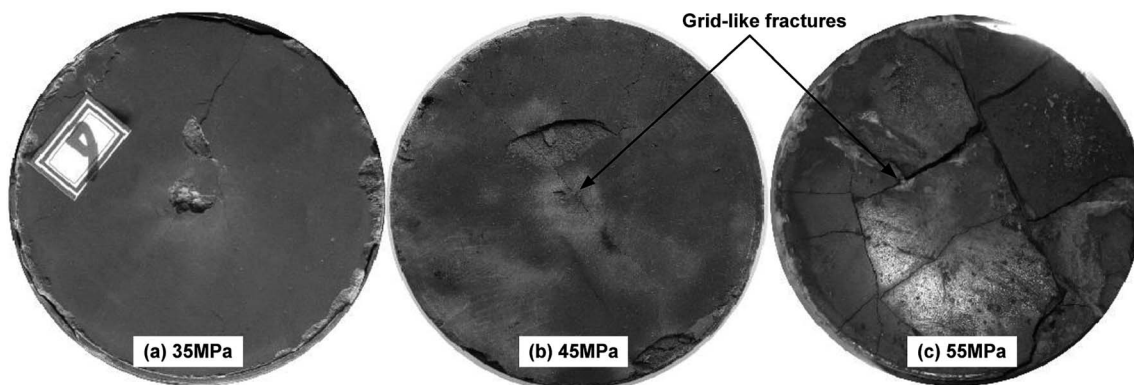| No.	Jet pressure (MPa)	Calculated peak pressure (MPa)	Core diameter (mm)	Core length (mm)	Impacting time (min)	Target distance (mm)	Temperature (°C)	Confining pressure (MPa)
1#	30	191	100	150–200	3	6	50	8
2#	35	210	100	150–200	3	6	50	8
3#	40	229	100	150–200	3	6	50	8
4#	45	247	100	150–200	3	1/3/6/9/12	50	8
5#	50	264	100	150–200	3	6	35/40/45/50/55	8
6#	55	282	100	150–200	3	6	50	8

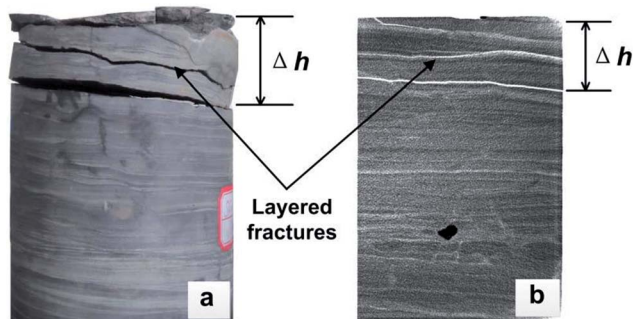Fig. 4   Pictures of head faces of shale-cores impacted by SC-CO$_2$ jet with different pump pressures.

Fig. 5   Failure of shale cores on the side face: (a) is the picture and (b) is the CT image.

pressure of SC-CO$_2$ jet, the broken depths of shale cores are much larger than those of marble cores but much smaller than those of man-made cores. It's analysed that this discrepancy is mainly caused by the combined actions of the mechanics strength and micro structures. In detailed, the compressive strength of the shale sample in this paper is about 45 MPa which is just between that of the man-made sample (25 MPa) and the marble sample (~65 MPa). In addition, the micro structure, such as the bedding and the grain composition, *etc.* is another key factor. On the whole, the broken depths are all approx-linearly increasing with the pressures of SC-CO$_2$ jet. On the other hand, the contrast experiments in Fig. 6 present that the broken depth of man-made cores by water jet is quite smaller than that by SC-CO$_2$ jet at the same pressure, which indicates that the rock breaking ability of SC-CO$_2$ jet is much more obvious than that of the water jet.

that the critical pump pressure for shale breaking is approximately 29.3. As comparison, the experimental results by Wang *et al.*[11] and Du *et al.*[23] are also presented in Fig. 6. For the same
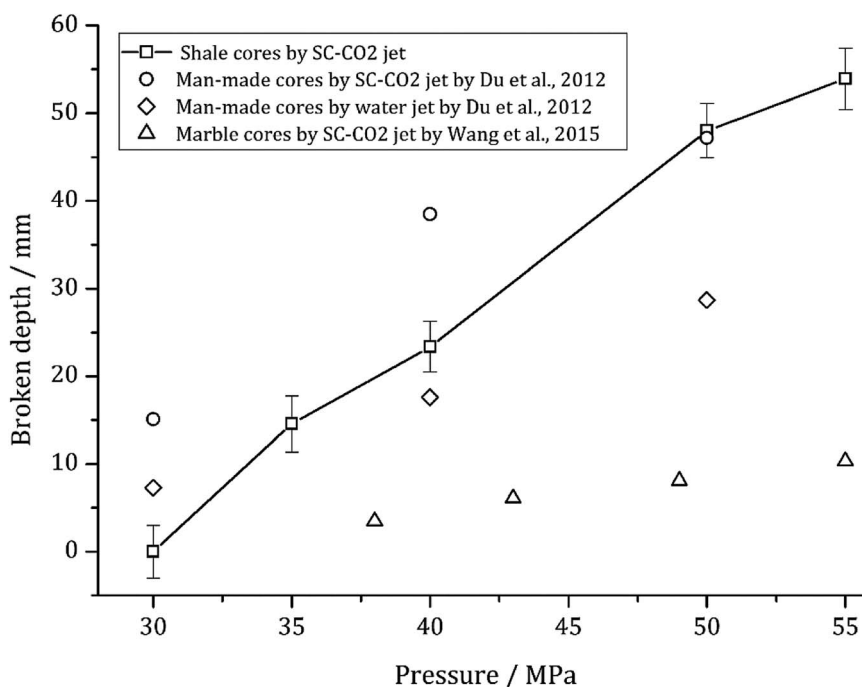

Fig. 6   Curves of broken depth and broken volume *vs.* pump pressure.

Fig. 7 illustrates the influence of target distance and temperature on the maximum broken depth of shale core plugs. Here, the target distance is defined as the axial distance between the SC-CO$_2$ jet outlet and the head surface of the shale core. The special experimental temperature is controlled by attemperation of the heater. A linearly increasing relationship between the maximum broken depth and the temperature is exhibited in Fig. 7. This trend indirectly indicates that the impact performance of the SC-CO$_2$ jet is positively dependent upon the temperature of the supercritical fluid. The maximum broken depth initially increases sharply with increasing target distance. However, it climbs to a peak value when the target distance increases to approximately 6 mm, above which the broken depth decreases with the target distance. This nonlinear relationship reveals that there may exist an optimal target distance giving a certain nozzle diameter. The impact performance of SC-CO$_2$ is most obvious at this distance. This trend can be explained by the structure of submerged jet. As known, the SC-CO$_2$ jet in this paper is a submerged jet. Its edge diffuses outwards after jetting from nozzle exit. Hence the diameter of jet will increase along the jet axis. On the other hand, the mean velocity of jet decreases from nozzle exit. Then the impact force is the product of cross-sectional area multiply by jet pressure which is proportional to the square of mean velocity. Giving the condition of jet diameter increasing while mean velocity decreasing at the same time, there may exist a point where the impact force is most large. In this experiment, a distance of about three times of the nozzle outlet diameter is found to be the optimal one. But this optimal target distance can be changeable with the jet diameter.

3.2. The microchanges of shale

Fig. 8 shows the scanning electron microscope (SEM) images of the shale samples before and after erosion with a magnification of 2000 times. According to the SEM images, quartz, calcite and some other minerals compose the basic skeleton of the shale. The clay minerals and other organic matter fill the voids. A small number of medium and large pores with sizes between 0.1 and 5 μm are observed (Fig. 8(a)). After erosion by the SC-CO$_2$ jet, the microscopic structure of the shale is significantly damaged. In detail, the amounts of clay mineral, organic matter and other filling materials are significantly reduced. The original pores are no longer obvious. Overall, the shale sample shows a disordered microstructure after erosion by SC-CO$_2$ jet (Fig. 8(b)).

Two factors may account for the microstructure change. First, the impact load of the SC-CO$_2$ jet acts as a key factor. The process of high-speed fluids impacting solids can be divided into two typical stages: the water hammer pressure stage and the stagnation pressure stage.[24] The water hammer pressure is usually dozens of times the stagnation pressure and is generally accepted as the cause of crack initiation. It can be described by the following expression without consideration of the tiny deformations of the solid:[25]

$$P_w = \rho C v \qquad (2)$$

where P_w is the water hammer pressure in MPa, and ρ, C and v are the fluid density, the velocity of the shock wave and the fluid velocity, respectively. According to eqn (2), the water hammer pressure of the SC-CO$_2$ jet can reach a magnitude of nearly 200 MPa when the pump pressure is 30 MPa (Table 2). This huge impact pressure is sufficient to crush the shale's mineral structure, resulting in physical damage to the original ordered microstructure. Therefore, the impact pressure may be the main factor for the disorder of shale's microstructure.

Second, CO$_2$ is corrosive in the presence of water. SEM studies show that CO$_2$ can cause significant corrosion damage
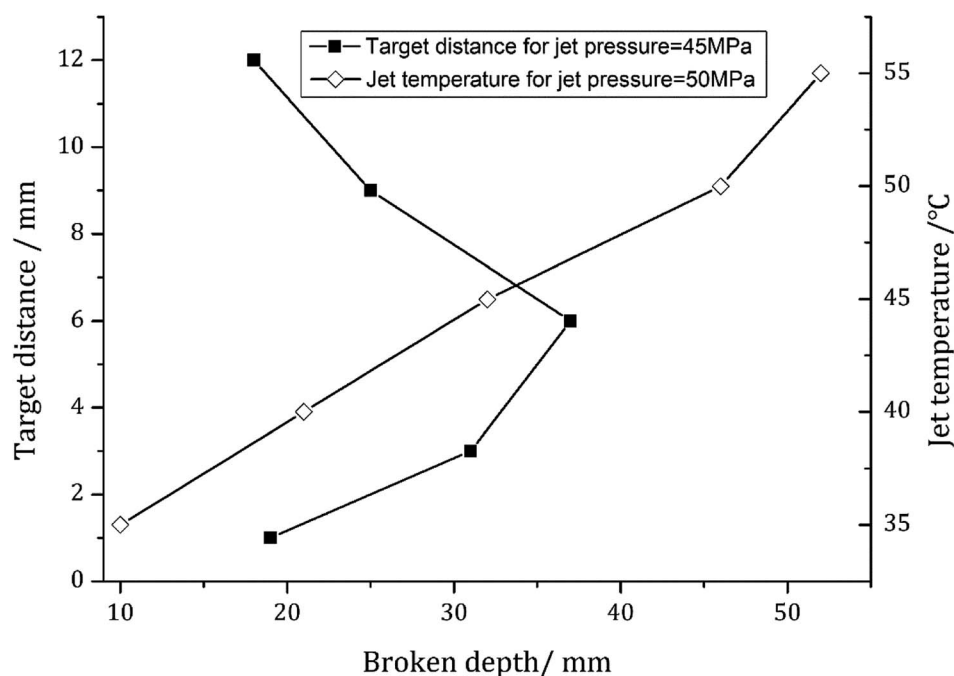

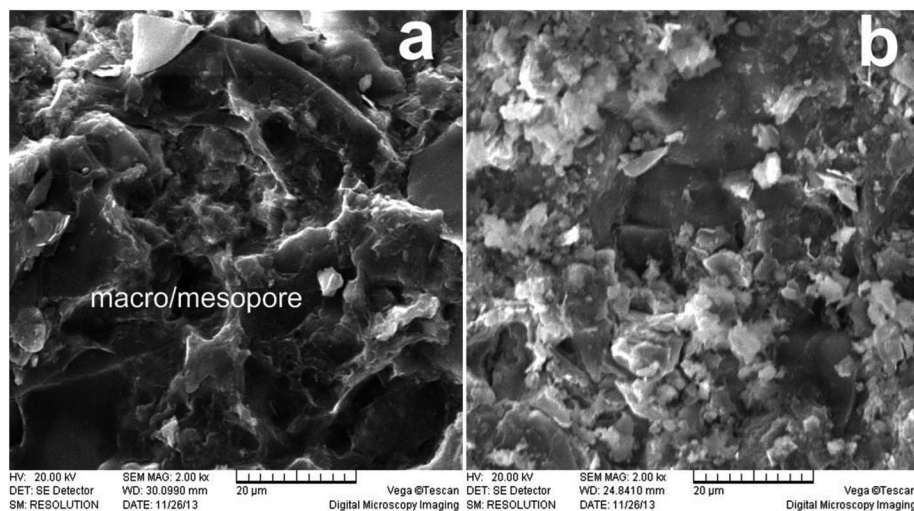**Fig. 7** Curves of broken depth *vs.* target distance and temperature.

Fig. 8 SEM images of original shale (a) and eroded shale (b).

Table 2 The percentage component of shale samples by means of X-ray fluorescence method

Shale samples	SiO_2	Al_2O_3	Fe_2O_3	K_2O	MgO	TiO_2	SO_3	CaO
Original shale	71.0364	14.9380	5.5275	3.9739	2.1151	1.1079	0.5372	0.3345
Eroded shale	70.0282	14.0077	5.4708	4.2188	1.6983	1.2722	0.5847	1.7832

to shale samples in high-pressure environments.[26] This shows that CO_2 mainly acts on clay minerals and organic matter. The literature[27] shows that the organic matter inside the shale decomposes upon exposure to SC-CO_2. Finally, the decomposition ingredients may block the original medium/large pores. Another literature[28] also shows that SC-CO_2 acts on the kerogen and causes the decomposition of organic debris during the extraction of petroleum from oil shale by means of supercritical fluid extraction. It is known that the activity of SC-CO_2 can be greatly enhanced in a high-temperature and high-pressure environment. This may promote the decomposition of organic matter in the shale while blocking the original pores and thus reducing the physical strength of the shale.[29] A contrast experiment was conducted to measure the mechanics change between natural and SC-CO_2 eroded shale samples at the same condition as in this paper.[30] It's presented that the tensile strength of shale sample eroded by SC-CO_2 decreases by 18.3% and the triaxial compressive strength by 8.3% respectively. Hence, it can be inferred that the erosion of SC-CO_2 fluid can reduce the mechanics strength of shale sample by changing its microstructure.

According to the above references, the clay minerals in shale may decompose as a result of the corrosion of SC-CO_2. Fig. 9 shows the XRD spectra of the shale samples. After erosion by the 30 MPa SC-CO_2 jet for 3 min, there was no change in the clay contents; after erosion by the 55 MPa SC-CO_2 jet for 3 min, the contents of illite and clinochlore decreased significantly, as shown in Fig. 9a. The CO_2 reacted with the pore water, and the

carbonic acid generated. Under high-temperature and high-pressure conditions, the acidic environment will cause the decomposition of illite and clinochlore.[31] In addition to the decomposition of clay minerals, an obvious decrease of dolomite can be observed according to the XRD spectra, as shown in Fig. 9b.

In natural shale gas reservoirs, the decomposition reaction of clay minerals affected by CO_2 may take a long time, even as long as several years. In this experiment, the decomposition duration of the clay minerals is significantly shortened. First, the physical impact of the high-speed SC-CO_2 jet may lead to the rapid decomposition of clay minerals. Then, the high temperature can accelerate the reaction of CO_2 with clay minerals.[32,33] However, due to the relatively short duration of the experiments, the decomposition of the clay minerals may not be complete, and changes of other minerals are not observed by semiquantitative XRD analysis.

X-ray fluorescence was used to analyze the changes of the shale components before and after the SC-CO_2 jet impacting. The exact percentage of some major component of shale samples is illustrated in Table 2. Fig. 10 is the histogram showing the contrast of components in shale samples before and after the SC-CO_2 jet impacting. The obvious decreases of aluminum oxide and magnesium oxide are observed in the histogram. These two oxides are the main components of clay minerals. The changes of these two oxides further strengthen the finding of clay mineral decomposition after the SC-CO_2 jet impacting. However, a large increase in calcium oxide is observed in Fig. 10. This increase has
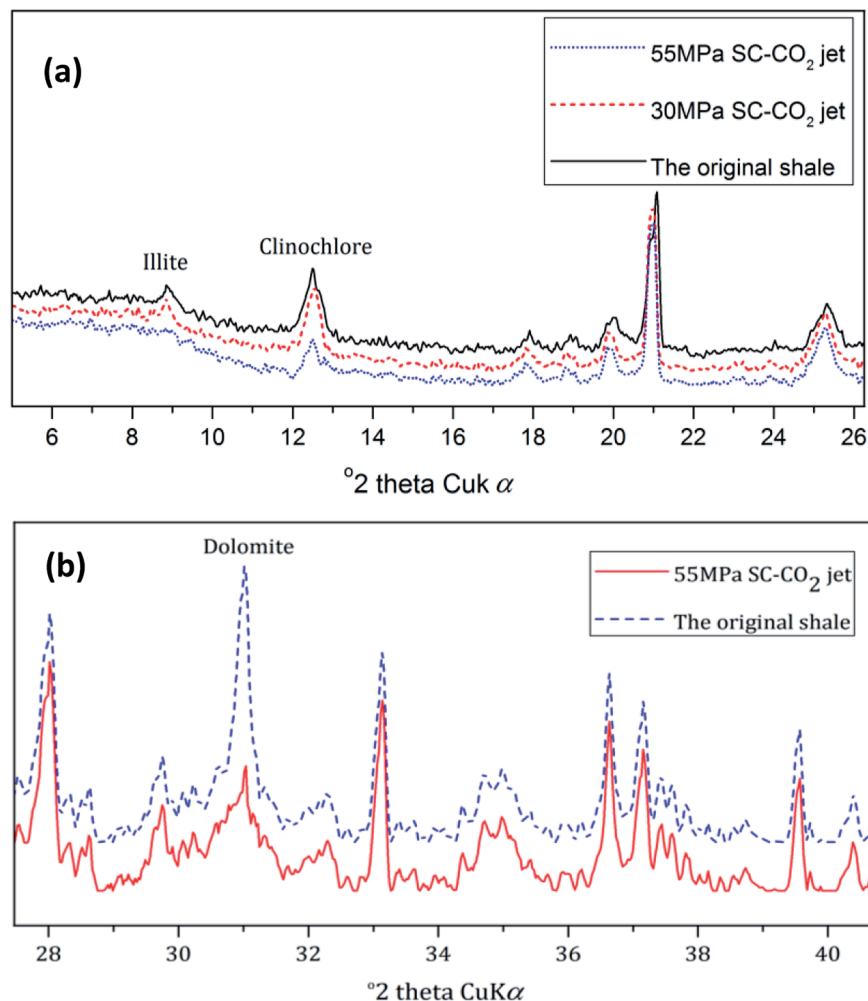
Fig. 9 Bulk XRD plot of the original shale and the eroded shale.

a close connection with the adsorption of carbon by shale samples, which is discussed in detail in the following section.

3.3. The adsorption of carbon on the shale surface

According to Fig. 4, multiple radial cracks were generated on the top surface. Along the radial cracks, multiple samples were selected equidistantly to test the carbon content. The relationship between the carbon content and the radial distance is shown in Fig. 11. A nonlinear fitting of the test data is shown in Fig. 11. It can be expressed as follows:

$$Pr = 0.56 + \frac{7.24}{1 + \exp(20 \times (r/r_0 - 0.43))} \tag{3}$$

where r is the radial distance and r_0 is the radius of the shale core. The fitting correlation coefficient of the formula is $R^2 = 0.9687$. According to the changing tendency of carbon content, the top surface can be divided radially into three areas. The circle from center to $0.25r_0$ is Area I. The average carbon content in this area is relatively high (*i.e.*, as high as 8%). It decreases slightly with increasing radial distance. Then, the annulus from $0.25r_0$ to $0.6r_0$ is Area II. The average carbon content in this area decreases

rapidly with increasing radial distance. The annulus from $0.6r_0$ to r_0 is Area III. The average carbon content in this area is relatively low. Within Area III, the carbon content tends to be a constant.

The change in carbon content indicates that the shale can absorb CO_2. A large number of studies have shown that shale has sequestration characteristics for supercritical, gaseous and liquid CO_2.[31,34,35] In previous experimental studies, CO_2 acted on shale in static form. The action duration of the CO2 was relatively longer. However, in this experiment, CO_2 was in the form of supercritical jets. In Fig. 10, Area I is the direct erosion area of the SC-CO_2 jet. Area II is the action area of the SC-CO_2 radial jet. Lastly, Area III is the action area of the SC-CO_2 back flow. According to the test data, the carbon content increases significantly when subjected to the direct erosion of the SC-CO_2 jet. This indicates that the interaction between the SC-CO_2 jet and the shale sample contributes to the adsorption of CO_2 in shale.

4. Discussion

According to the studies by Kolle and Du *et al.*, the method of rock breaking by SC-CO_2 jet has the advantages of low threshold
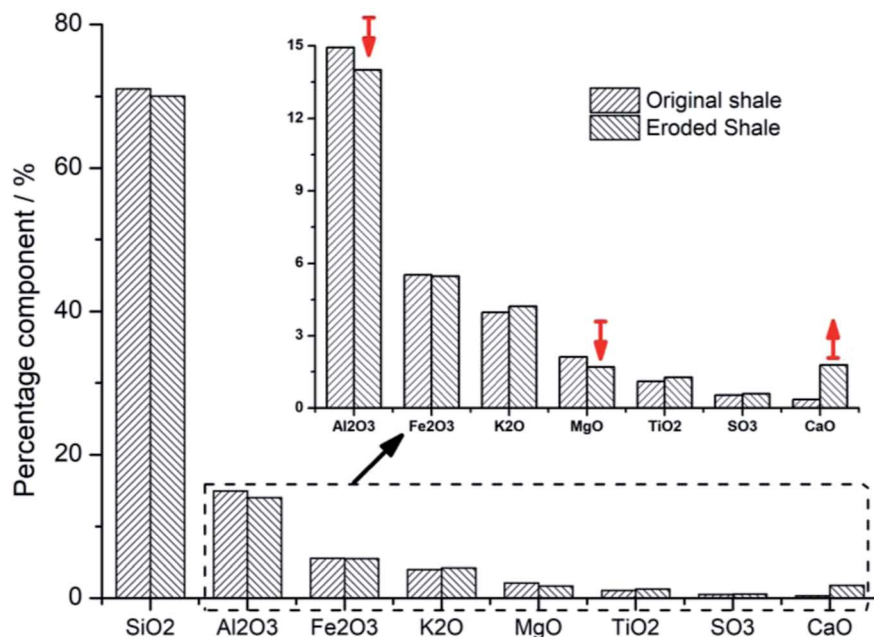
Fig. 10 Contrast of components in shale samples before and after the SC-CO_2 jet impacting.
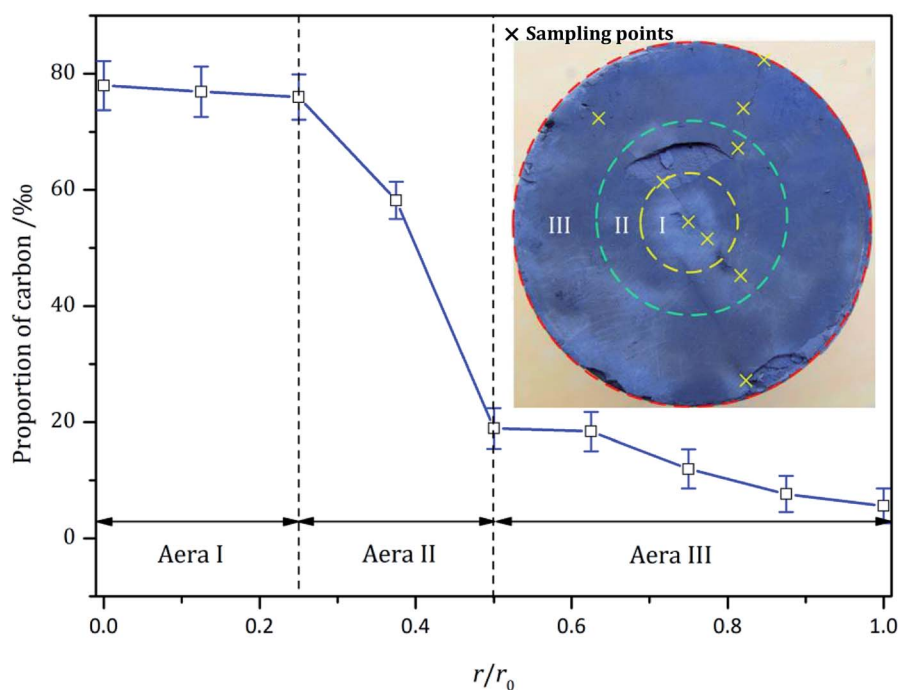

Fig. 11 Proportions of carbon on the head face of shale-core.

pressures and volume breakage.[8,10] It is inferred that the combined action of three main factors may cause the shale-breaking phenomenon. They are the jet impact load, the corrosion properties of CO_2 at high-temperature and under high-pressure conditions, and the bedding characteristics of shale.

First, the impact load of the SC-CO_2 jet is the dominant factor leading to shale breakage. It is known that the water hammer pressure induced at the initial stage by the impact load spreads radially in the form of stress waves. These waves include the Rayleigh wave and the body wave (*i.e.*, longitudinal and transverse waves).[36,37] According to eqn (2), the water hammer pressure can reach a magnitude near 0.2 GPa (Table 2). On the shale surface, the Rayleigh waves produce a shear stress component and a tensile stress component.[38] These large shear stress components and tensile stress components first induce
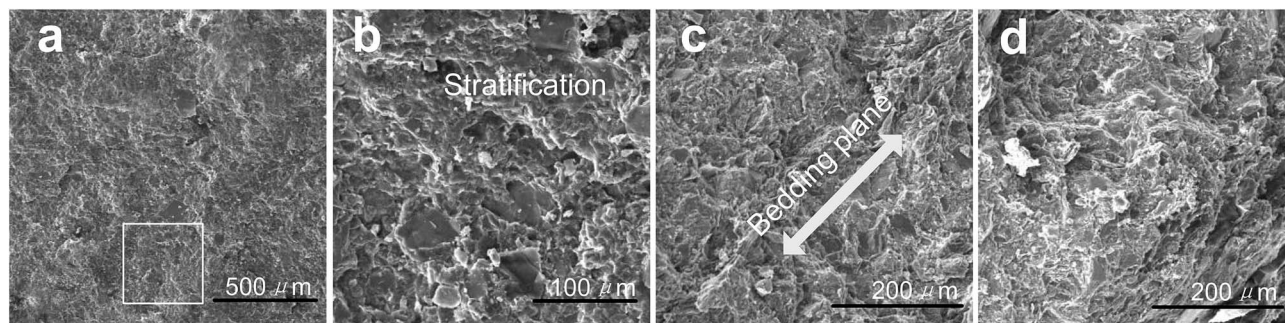
Fig. 12 SEM images of fracture surface of shale samples; (a) and (b) are the surface of transverse fractures with the magnification of ×100 and ×500; (c) and (d) are the surface of longitudinal fractures with the magnification of ×300 and ×300.

the generation of initial cracks on the shale surface. As a result, the propagation of Rayleigh waves may account for the grid-like fragmentation phenomenon on the shale surface.

Second, the water hammer pressure spreads inside the shale in the form of spherical stress waves. It is known that the reflection of waves could enhance the tensile stress in certain areas inside the shale. The tensile strength of the shale is much lower than the compressive strength (Table 1). Therefore, initial cracks will be generated in these enhanced areas. Then, it can be observed that multiple beddings are nearly parallel to each other from the CT images in Fig. 1. These beddings further weaken the tensile strength of the shale sample and cause the initial cracks to extend along the bedding planes under tensile stress. This is the direct cause for the macroscopically visible transverse cracks seen in Fig. 5. The SEM method is applied to investigate the foregoing assumptions. It can be observed from the SEM images that the surfaces of transverse cracks are stratified. This stratification agrees with the typical character of tensile fracture (Fig. 12(a) and (b)). On the other hand, the surfaces of longitudinal cracks are disordered (Fig. 12(c) and (d)). These cracks may be the result of shear stress.

Third, from the SEM images and XRD semiqualitative analysis, it can be seen that $SC\text{-}CO_2$ fluid has changed the microscopic structures and the component compositions of shale material. Therefore, it can be inferred that the physical and mechanical strength of shale samples could be weakened after erosion. Shale erosion occurs in the area where it is directly subjected to the $SC\text{-}CO_2$ jet. Thus, the breakage of shale samples in this area is much easier. The grid-like fragmentation phenomenon may be the result of erosion.

5. Conclusions

According to the experimental studies, $SC\text{-}CO_2$ jet could effectively promote the decomposition of clay minerals. Meanwhile, the jet impact could change the microstructures of shale samples. According to the change laws of carbon content on the shale surface, the shale sample could absorb supercritical CO_2. The shale sample takes on the phenomenon of massive layered breakage subjected to the $SC\text{-}CO_2$ jet. This could be caused by the following key factors. First, the stress wave induced by the dynamic load of the $SC\text{-}CO_2$ jet impact is the dominant factor.

Then, the erosion of shale samples by $SC\text{-}CO_2$ under high-pressure and high-temperature environments is an auxiliary factor. Third, the parallel bedding feature of the shale sample is the internal factor. However, due to the restrictions of the core plug sizes and the pump pressures, the above findings may have certain limitations. Subsequent experimental studies will be conducted to supplement the existing results. Overall, the method of $SC\text{-}CO_2$ jet breaking shale is valid and feasible.

Conflicts of interest

There are no conflicts to declare.

Acknowledgements

References

1 S. Gou, T. Yin, Q. Xia and Q. Guo, *RSC Adv.*, 2015, **5**, 32064–32071.
2 W. Chen, C. Zou, X. Li and L. Li, *RSC Adv.*, 2016, **6**, 90682–90689.
3 J. Xu, Z. Qiu, X. Zhao, T. Mou and H. Zhong, *RSC Adv.*, 2018, **8**, 20852–20861.
4 Y. Xuan, G. Jiang, Y. Li and X. Zhang, *RSC Adv.*, 2015, **5**, 84947–84958.
5 Phase diagram of carbon dioxide, Source: https://www.chemicalogic.com.
6 H. Sun, W. Sun, H. Zhao, Y. Sun and D. Zhang, *RSC Adv.*, 2016, **6**, 32770–32778.
7 P. J. Jarboe, P. A. Candela, W. L. Zhu and A. J. Kaufman, *Energy Fuels*, 2015, **29**, 7897–7909.
8 H. Wang, G. Li and Z. Shen, *Energy Sources*, 2012, **34**, 1426–1435.
9 J. J. Kolle, *SPE J.*, 2000, 65534.
10 Y. K. Du, R. H. Wang, H. J. Ni and M. K. Li, *Journal of Hydrodynamics*, 2012, **24**, 554–560.

11 H. Wang, G. Li, Z. Shen, S. Tian and B. Sun, *J. Pet. Sci. Eng.*, 2015, **127**, 305–310.

12 Q. Li and M. Jing, *Chin. J. Rock Mech. Eng.*, 2013, **32**, 2205–2213.

13 X. Guo, H. Ni, M. Li, L. Zhang and Y. Wang, *Indian Geotech. J.*, 2018, **48**, 1–8.

14 X. Zhang, Y. Lu, J. Tang, Z. Zhou and Y. Liao, *Fuel*, 2016, **190**, 370–378.

15 Y. Hu, Y. Liu, C. Cai, Y. Kang and X. wang, *Appl. Sci.*, 2017, 7, 1093.

16 Y. Lu, X. Ao, J. Tang, Y. Jia and X. Zhang, *J. Nat. Gas Sci. Eng.*, 2016, **30**, 268–275.

17 S. Zhang, X. Xian, J. Zhou and L. Zhang, *RSC Adv.*, 2017, 7, 42946–42955.

18 S. Chen, Y. Zhu, H. Wang, H. Liu and W. Wei, *Energy*, 2011, **36**, 6609–6616.

19 X. Zhao, J. Kang and B. Lan, *Renewable Sustainable Energy Rev.*, 2013, **21**, 603–613.

20 C. Yue, S. Li, H. Wen, F. Yang and X. Xu, *RSC Adv.*, 2018, **8**, 6436–6443.

21 M. Nasseri, F. Rezanezhad and R. Young, *Int. J. Fract.*, 2011, **168**, 1–13.

22 A. W. Momber, *Wear*, 2004, **256**, 1190–1195.

23 Y. K. Du, R. H. Wang, H. Ni, H. J. Huo, Z. Huang, W. Yue, H. Zhao and B. Zhao, *J. China Univ. Petrol.*, 2012, **36**, 93–96.

24 J. E. Field, *Wear*, 1999, **233**, 1–12.

25 S. S. Cook, *Proc. R. Soc. London, Ser. A*, 1928, **119**, 418–488.

26 R. Lahann, M. Mastalerz, J. Rupp and A. Drobniak, *Int. J. Coal Geol.*, 2013, **108**, 2–9.

27 M. Angeli, M. Soldal, E. Skurtveit and E. Aker, *Energy Procedia*, 2009, **1**, 3351–3358.

28 M. Allawzi, A. Al-Otoom, H. Allaboun, A. Ajlouni and F. A. Nseirat, *Fuel Process. Technol.*, 2011, **92**, 2016–2023.

29 T. F. Xu, J. A. Apps and K. Pruess, *Chem. Geol.*, 2005, **217**, 295–318.

30 J. Tang, Y. Lu, Y. Chen, X. Zhang, X. Ao, Y. Jia and Q. Li, *Rock Soil Mech.*, 2018, **39**, 797–802.

31 B. L. Alemu, P. Aagaard, I. A. Munz and E. Skurtveit, *Appl. Geochem.*, 2011, **26**, 1975–1989.

32 C. Fouillac, B. Sanjuan, S. Gentier and I. Czernichowski-Lauriol, *Third Annual Conference on Carbon Capture and Sequestration*, Alexandria, VA, May 3–6, 2004.

33 A. Busch, S. Alles, Y. Gensterblum, D. Prinz and D. N. Dewhurst, *Int. J. Greenhouse Gas Control*, 2008, **2**, 297–308.

34 J. Wollenweber, S. Alles, A. Busch, B. M. Krooss and H. Stanjek, *Int. J. Greenhouse Gas Control*, 2010, **4**, 231–241.

35 T. R. Elliot and M. A. Celia, *Environ. Sci. Technol.*, 2012, **46**, 4223–4227.

36 F. P. Bowden and J. E. Field, *Proc. R. Soc. London, Ser. A*, 1964, **282**, 331–352.

37 Y. Zhao, L. Zhang, W. Wang, W. Wan and S. Li, *Rock Mech. Rock Eng.*, 2017, **50**, 1–16.

38 M. V. Swain and J. T. Hagan, *J. Mater. Sci.*, 1980, **15**, 387–404.